IEEE Access
Multidisciplinary | Rapid Review | Open Access Journal

Received January 24, 2021, accepted January 26, 2021, date of publication January 29, 2021, date of current version February 8, 2021.

Digital Object Identifier 10.1109/ACCESS.2021.3055547

A Study on Stability Boundary of Highly Flexible Aircraft With Saturation Constraint

LIANG XU[1], (Member, IEEE), RUI CAO[1], YANBIN LIU[2], AND YUPING LU[1]
[1]College of Automation Engineering, Nanjing University of Aeronautics and Astronautics, Nanjing 211106, China
[2]Academy of Astronautics, Nanjing University of Aeronautics and Astronautics, Nanjing 211106, China

Corresponding author: Yanbin Liu (nuaa_liuyanbin@139.com)

This work was supported in part by the Jiangsu Innovation Program for Graduate Education under Grant KYLX15_0272, in part by the Fundamental Research Funds for the Central Universities, and in part by the National Natural Science Foundation of China under Grant 11572149.

ABSTRACT This paper deals with investigating the closed-loop stability boundary of the highly flexible aircraft with structural flexibility and input saturation constraint. A method is presented to analyze the stable region based on the system features of the open-loop instability. In this paper, a dynamic model of highly flexible aircraft is made and the dynamic characteristics are analyzed and the long period mode and stability are investigated in terms of the trimmed model. Considering the saturation constraint of elevator deflection, the closed-loop stability boundary of the system under saturation constraint is discussed by combining the open-loop instability features of highly flexible aircraft. The analysis indicates that the boundary is related to the left eigenvector consistent with the amplitude constraint and the unstable poles of the control signals. Based on the long period instability of the aircraft, the formula of closed-loop stability boundary is analytically obtained. The convergence region of highly flexible aircraft is verified in terms of the LQR controller. The influence of structural flexibility and saturation constraint amplitude of elevator on the stability boundary of highly flexible aircraft is analyzed based on state constraints, which is also compared with the rigid aircraft. The simulation results show that the closed-loop stability of the system is restricted by the open-loop characteristic of the system and the control input saturation constraint.

INDEX TERMS Highly flexible aircraft, stability boundary, saturation constraint.

I. INTRODUCTION

High-altitude long-endurance (HALE) aircraft are able to continuously collect and transmit data in real time. They can be used extensively in military and civilian applications, such as communication support, disaster monitoring, environmental research, and meteorological data monitoring, attracting a great deal of interest [1], [2]. Perfect high-altitude long-endurance aircraft can maintain a high altitude of over 20,000 meters for several months. They need to have a lift-drag ratio that is as large as possible to decrease energy consumption and to achieve the objective of staying at high altitudes for a long time. Hence, this type of aircraft has a very large wing aspect ratio, and its structure must be very light. Because of their slenderness, the wings may undergo large deformations under normal conditions, resulting in geometrically nonlinear behavior. Therefore, these wings have a highly flexible structure [3], [4].

In the past several years, many scholars have carried out many studies on large-scale flexible aircraft, including nonlinear aeroelastics [5]–[8], coupling dynamics modeling [9], [10], model reduction [11], [12], stability analysis [13], [14], trajectory tracking [1], [15], flutter suppression and gust alleviation [16]–[18]. These studies strongly promote investigations of the dynamic characteristics of highly flexible aircraft. Based on the results of highly flexible aircraft model analysis, one of the main problems in the control system design is to ensure the closed-loop stability of the aircraft when actuator saturation constraints exist [19], [20]. When there are unstable poles in the open-loop system, the conditions of closed-loop stability are more stringent. Therefore, it is necessary to consider the effect of the open-loop features on the closed-loop control performance to promote the preliminary design of aircraft with a more reliable control performance.

The associate editor coordinating the review of this manuscript and approving it for publication was Rosario Pecora.

In numerous controller design methods of current control theory, it is assumed that the system control input can be infinitely large, which ignores the saturation constraints of the actuator [21], [22]. In the real control design and engineering process, the input constraints and model uncertainties limit the aircraft in achieving a perfect control performance [23]–[25]. Hence, based on ideal assumptions, the closed-loop performance of the designed control system may not be completely guaranteed [26], [27]. The actuators of highly flexible aircraft are conventional control mechanisms such as elevators that are normally limited by the response bandwidth and saturation constraints. Therefore, it is essential to analyze the stability performance of the aircraft system, design the control system reasonably, and investigate the stability boundary in order to reach the performance limit of the system in terms of these actuator constraints [28].

For systems with saturation constraints, the concept of the domain of attraction was proposed to approximate the system performance [29]. Previously, Schmitendorf and Barmish *et al.* investigated the null controllability of linear systems under control saturation constraints. They provided the sufficient and necessary conditions for global controllability under constraints and the necessary and sufficient circumstances for the existence of admissible control considering that a given initial point can return to the origin in finite time [30]. In analyzing the stabilization problem of unstable systems, Goman and Demenkov proposed that determining the size of the controllable region is the key to studying control saturation, and the size of this region can be considered a measure of the allowable level of external disturbance [31].

In the study of designing discrete control systems, Kouvaritakis *et al.* proposed necessary and sufficient conditions for bounded input/bounded output (BIBO) stability in discrete systems [32]. In addition, it was noted that the stability condition is consistent with the physical constraints of the open-loop stabilization system. However, an unstable system needs much stronger constraints, according to which the conditions for guaranteeing the stability of the closed-loop system can be considered. Moreover, Derong Liu and A. N. Michel provided sufficient conditions for the null controllability of discrete-time linear systems under certain conditions of the input and state constraints [33]. Furthermore, Corradini *et al.* proposed an iterative characterization of the null controllable region for discrete-time linear systems with unstable eigenvalues [34].

To analyze the continuous-time control system, Tingshu Hu investigated the accessibility of the inverse time system of the state equation under admissible control signals. In addition, the concrete form of the null controllable region was defined by the form of a set of extremum trajectories for unstable systems [35]. Meanwhile, focusing on a high-order system with two unstable poles, a linear feedback saturation controller was designed to verify that the attraction domain of the closed-loop feedback system can only be a subset of the null controllable region [36]. Moreover, Lin *et al.* converted the solution of the contraction ellipse invariant set under the saturation constraint to a linear matrix inequality (LMI) constraint optimization problem to straightforwardly obtain the system convergence domain [37].

The majority of studies on null controllable regions under saturation constraints are focused on linear systems. For instance, assuming a lack of uniform controllability for a group of time-dependent linear control systems, Fabbri *et al.* investigated the dimension, topological structure, and other dynamical features of the sets of null controllable points and reachable point sets [38]. Darup and Monningmann presented a technique for the exact computation of null controllable sets for single-input bilinear systems with input and state constraints [39]. In comparison with linear systems, much less research exists on the null controllable regions of nonlinear systems. A method was presented by Homer *et al.* for the control of input-constrained nonlinear systems that provided guaranteed stabilization in the entire null controllable region [40], [41]. Nonlinear systems are more difficult to study and require more attention [42], [43].

The influence of flexibility on the stability of aircraft was discussed in previous studies, and numerous performance optimizations were presented for the system [6], [44], [45]. Nevertheless, the influence of flexibility on controllability was not studied specifically, particularly under saturation constraints. This article proposes a method of analyzing the effect of control saturation and structural flexibility on the stability radius of highly flexible aircraft. The computational formula of the closed-loop stability boundary is provided based on the long-period instability features of highly flexible aircraft. With the performance limitations incorporated into the design phase, another method is provided to increase the controllability of highly flexible aircraft.

This paper studies the stability boundary of highly flexible aircraft with structural flexibility and input saturation constraints. In general, the main contributions include the following.

1) An approach is proposed to analyze the influence of control saturation and structural flexibility on the stable radius of highly flexible aircraft. According to the long period instability characteristics of highly flexible aircraft, the computational formula of closed-loop stability boundary is given.
2) With the performance limitations incorporated into the design phase, this paper brings one more way to broaden the controllability of highly flexible aircraft.

The paper is organized as follows: a dynamic model of highly flexible aircraft is constructed, and the dynamic characteristics are analyzed in Section II. Based on the trimmed model, the stability and long-period mode are studied. In Section III, by studying the null stability boundary and controllability of the 1st-order and 2nd-order unstable modes, the influence of the saturation constraints on the local stability of the closed-loop system is discussed. Next, the stability boundary of highly flexible aircraft is provided. In Section V, the effect of the structural flexibility and saturation constraint

amplitude of the elevator on the stability boundaries of highly flexible aircraft is analyzed and compared with that of rigid aircraft. Finally, concluding remarks are given in Section V.

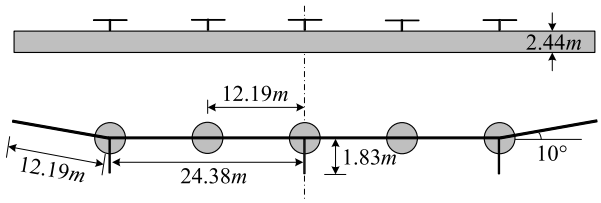

FIGURE 1. The geometry of the flying wing model.

II. DYNAMIC MODEL OF HIGHLY FLEXIBLE AIRCRAFT

The object of this study is a flying wing flexible aircraft, the geometric model of which is shown in Figure 1. The wing length of this flying wing flexible aircraft is 72.8 m with a half-chord length of 2.44 m. The outboard, one-third of the wing semispan, has a dihedral angle of 10°. Five propulsive units exist, with three pods located at the middle span and one at two-thirds of the semispan on each side. The pods in the center of the aircraft have masses of 27.23 kg, within the range of 0 (light) to 227 kg (heavy). The pods on the edges have masses of 22.70 kg. The properties of the aircraft are listed in Table 1 [46]. The aerodynamic derivatives $C_{l\alpha}$, $C_{l\delta}$, C_{d0}, C_{m0}, and $C_{m\delta}$ are all in units of rad^{-1}. The L.E. is the abbreviation of leading edge.

TABLE 1. Relevant properties of the flying wing.

Structural/ Aerodynamic Property	Value
Cross-sectional elastic axis	25% chord from L.E.
Cross-sectional center of gravity	25% chord from L.E.
Bending stiffness (EI_x)	1.03×10^6N·m^2
Torsional stiffness (GJ)	1.65×10^5N·m^2
Chordwise bending stiffness (EI_z)	1.24×10^7N·m^2
Compressive stiffness (EA)	1×10^{10}N
Damping coefficient (c)	0.02
Mass per unit length (ρA)	8.93kg/m
Flatwise bending mass moment of inertia (I_{xx})	0.69kg·m
Torsional mass moment of inertia (I_{yy})	4.15kg·m
Chordwise bending mass moment of inertia (I_{zz})	3.46kg·m
$C_{l\alpha}$ for wings (25% chord)	2π
$C_{l\delta}$ for wings (25% chord)	1
C_{d0} for wings (25% chord)	0.01
C_{m0} for wings (25% chord)	0.025
$C_{m\delta}$ for wings (25% chord)	-0.25
$C_{l\alpha}$ for pods (25% chord)	5
C_{d0} for pods (25% chord)	0.02
C_{m0} for pods (25% chord)	0

In this study, a coupling dynamic model of highly flexible aircraft is constructed based on the finite element method and Lagrange equation by combining the fully geometrically exact model of nonlinear flexible beams and the unsteady aerodynamic model. In contrast to the traditional finite element model, this model considers the spanwise expansion deformation of a highly flexible wing and the coupling with the spanwise bending deformation. The model can reflect the interaction among the flight dynamics, structural dynamics, and aerodynamics of highly flexible aircraft well [47]. For the structural model, Euler-Bernoulli beam model equations are used to describe the characteristics of the slender flexible structures. For easier study, the kinetics of the three-dimensional beam are simplified into one-dimensional nonlinear beam motion and two-dimensional beam deformation. Based on the finite element method, the motion of each structural node is described by its displacement and velocity along three axes. After dividing the wing into n finite elements, the system states are defined as

$$\mathbf{x} = \left[\, V_x \;\; V_z \;\; q \;\; \theta \;\; h \;\; dsp_i(1:nf) \;\; vel_i(1:nf) \,\right]^T \tag{1}$$

where V_x and V_z are the horizontal velocity and vertical velocity of the center of mass, respectively. The velocity V, the rate of pitch angle q, the pitch angle θ and the altitude h express the rigid-body motion of highly flexible aircraft. The value of nf is related to the finite element number n, and the equation can be described as $nf = (n+1)\times 3$. The motion of each node is given in terms of the nodal displacement and velocity along the three axes. These are denoted as dsp_i and vel_i, respectively.

The control input of a large flexible aircraft is defined as $u_{2\times1} = [\delta_e \; \delta_T]$, where δ_e and δ_T are the elevator angle and thrust input, respectively.

In real flight, flexible deformation and elastic vibration mean that the wing is affected by unsteady aerodynamic forces. Based on the structural characteristics of slender flexible beams, the unsteady aerodynamic loads used in the current study are based on the 2-D finite state inflow theory provided in [48], [49]. This theory calculates aerodynamic loads on a thin airfoil section undergoing large motions in an incompressible inviscid subsonic flow [46].

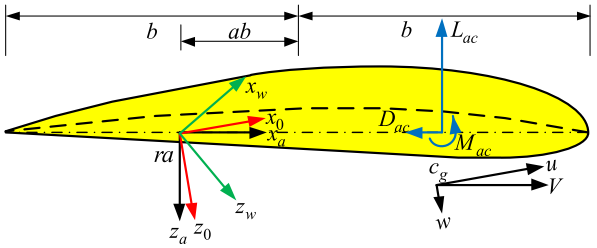

FIGURE 2. Local airfoil aerodynamic schematic.

Figure 2 presents a two-dimensional thin airfoil. b is the semi-chord length, ab is the distance of the mid-chord in front of the reference axis ra, and a is the percentage of ab in the semi-chord. The reference axis ra after the midpoint is defined as positive, and thus the motion of the wing can be described as the variational displacement h (where down is positive) and pitch angle displacement α (where up is positive) of point ra.

Based on the Grossman theory of unsteady aerodynamic forces and [49], the lift L_{c_g}, drag D_{c_g} and pitching moment M_{c_g} can be given by

$$\begin{aligned} L_{c_g} &= C_{l_\alpha}\rho V^2 b[\alpha + \frac{\dot{h}}{V} + (\frac{1}{2} - a)b\frac{\dot{\alpha}}{V}] + C_{l_{\delta_a}}\rho V^2 b\delta_a \\ M_{c_g} &= (\frac{1}{2} + a)bL_{c_g} - \frac{1}{2}\pi\rho V b^3\dot{\alpha} + 2\rho V^2 b^2(C_{m_0} + C_{m_{\delta_a}}\delta_a) \\ D_{c_g} &= \rho b V^2 C_{d_0} \end{aligned} \tag{2}$$

where δ_a is the angle of deflection of the aileron surface and C_{l_α} is the slope of the lift curve. $C_{l_{\delta_a}}$ is the slope of the lift curve, and $C_{m_{\delta_a}}$ is the slope of the pitching moment, both of which are determined by the control surface. C_{d_0} and C_{m_0} directly represent the resistance coefficient and pitching moment of zero incidence.

The nonlinear dynamic model of highly flexible aircraft is derived based on the Lagrange method. The kinetic energy, potential energy and generalized external forces are summed across all wing elements. Additionally, the kinetic energy indicates the translational, rotational and elastic oscillations of the wing structure as well as the coupling action among them. The potential energy includes the bending, stretching and torsional deformation potential energy of the wing structure. The dynamic equations of the system can be written as follows [47]:

$$\begin{aligned} &\begin{bmatrix} M_{BB}(p) & M_{BF}(p) \\ M_{FB}(p) & M_{FF} \end{bmatrix}\begin{bmatrix} \dot{\boldsymbol{\beta}}_g \\ \ddot{\boldsymbol{p}} \end{bmatrix} + \begin{bmatrix} \mathbf{0} & \mathbf{0} \\ \mathbf{0} & K_{FF} \end{bmatrix}\begin{bmatrix} \mathbf{b}_g \\ p \end{bmatrix} \\ &\quad + \begin{bmatrix} C_{BB}(p, \boldsymbol{\beta}_g) & C_{BF}(\dot{\boldsymbol{p}}, p, \boldsymbol{\beta}_g) \\ C_{FB}(p, \boldsymbol{\beta}_g) & C_{FF}(\boldsymbol{\beta}_g) \end{bmatrix}\begin{bmatrix} \boldsymbol{\beta}_g \\ \dot{\boldsymbol{p}} \end{bmatrix} \\ &\quad = \begin{bmatrix} Q_{BB}(\dot{\boldsymbol{p}}, p, \boldsymbol{\beta}_g) \\ Q_{FF}(\dot{\boldsymbol{p}}, p, \boldsymbol{\beta}_g) \end{bmatrix} \end{aligned} \tag{3}$$

where M_{BB}, M_{BF}, M_{FB}, and M_{FF} are the components of the generalized mass matrix. C_{BB}, C_{BF}, C_{FB}, and C_{FF} represent the generalized damping. K_{FF} is the generalized stiffness matrix. b_g describes the linear and angular displacements. β_g represents the linear and angular velocities. p is related to the strain on each finite element. Q_{BB} integrates the external moments and external forces; however, Q_{FF} represents the generalized force acting on the wing.

In contrast to conventional aircraft, the nonlinear dynamic model adds the factors of wing deformation, which bring additional alterations in the aerodynamic characteristics. Moreover, the unique flight motion will in turn affect the wing deformation.

Trimming is performed by iterative calculations, which consider the coupling of aerodynamic force calculations and structural finite element static force analysis. In each iterative calculation, first, the aerodynamic model is updated based on the deformation results of the last calculated structure. Second, on the basis of the deformed configuration, the trim parameters are calculated (such as the angle of attack of the rigid body α, angle deflection of the control surface δ, and thrust T), and aerodynamic loads are obtained under related conditions. Last, letting the trimming loads act on the undeformed structure and setting the deformation level as the criterion of iterative convergence, convergent trimming results can be obtained. The trimming process is shown in Figure 3.

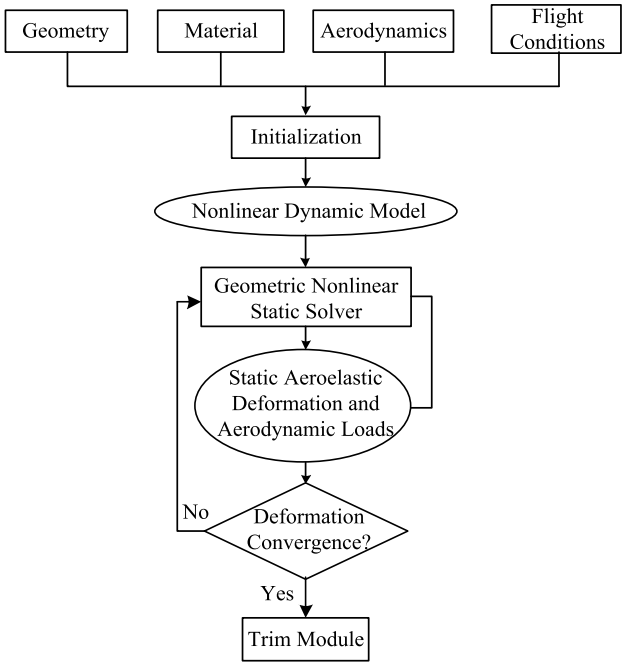

FIGURE 3. Block diagram of trimming process.

TABLE 2. The trim results of the flying wing aircraft.

Payload	Model	Angle of attack(°)	Elevator deflection(°)	Thrust per motor(N)
Light	Present	3.06	5.7	37.4
	NATASHA	3.11	5.68	37.4
	UM/NAST	3.1	5.68	37.2
	NWPU/ZZ	3.1	5.7	37.3
	BUAA/ZJ	3.08	5.69	37.38
Heavy	Present	4.85	0.57	37.95
	NATASHA	4.92	0.56	37.65
	UM/NAST	4.86	0.47	37.32
	NWPU/ZZ	4.9	-0.4	45.5
	BUAA/ZJ	4.88	0.56	37.10

The nonlinear dynamic model is trimmed by calculating the coupling iteration of the static aeroelastic deformations and aerodynamic load to assess the effect of the payload on the stability of the flexible aircraft. The highly flexible aircraft is set to fly at a speed of 12.19 m/s at sea level, and the angle of attack, thrust of the balanced state, and elevator deflection are trimmed and are shown in Table 2. The table lists the trimmed findings for this aircraft with the other four authoritative teams. Patil *et al.* established the computing package of the Nonlinear Aeroelastic Trim and Stability of HALE Aircraft (NATASHA) [50]. The University of Michigan's Nonlinear Aeroelastic Simulation Toolbox (UM/NAST) was developed by Professor Cesnik and collaborators [46]. NWPU/ZZ was proposed by Professor

Zhou Zhou and collaborators at Northwestern Polytechnical University [3]. Professor Jinwu Xiang and collaborators at Beihang University used BUAA/ZJ to determine the calculation result [51]. Figures 4-7 show the variations in the trimmed angle of attack, elevator deflection, and thrust per motor with different payloads. The figures also present the trimmed results for rigid aircraft under the same circumstances. The heavier the payload is, the higher the lift required. Thus, the required angle of attack and lift increase by increasing the payload.

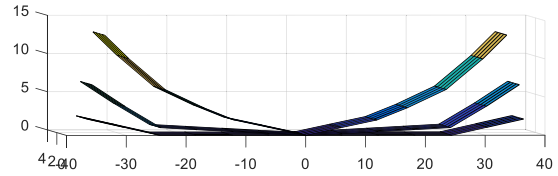

FIGURE 4. The deformed image of the trim aircraft with different payloads.

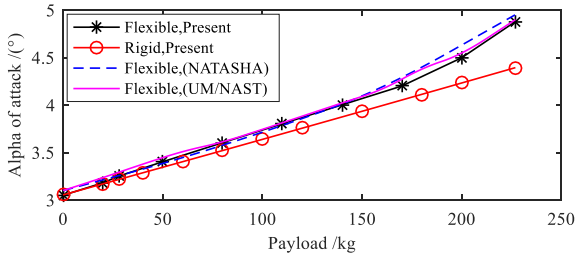

FIGURE 5. The trim angle of attack with a varying payload mass.

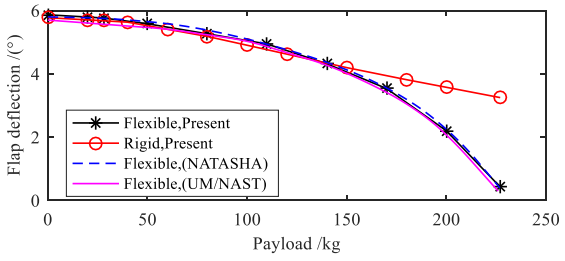

FIGURE 6. The trim elevator deflection with a varying payload mass.

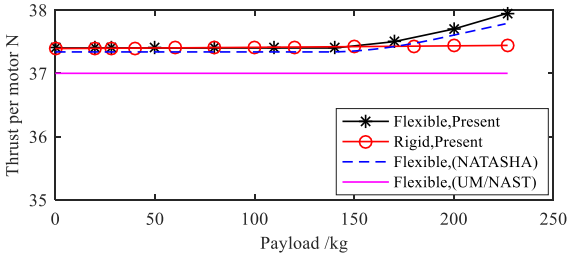

FIGURE 7. The trim thrust per motor with a varying payload mass.

Figure 4 shows a comparison of the deformed shapes of the trim aircraft with payloads of 0 kg (light), 120 kg, and 227 kg (heavy). The trim shapes in these cases are very different, even though the flight conditions, material and inertial properties of the three models are identical [52]. In the case of the 227 kg configuration superimposed on the undeformed shape, the bending displacement of the wing tip reaches 13.11 m, which reflects its high flexibility.

The lateral aerodynamic component of the outer wing segment gradually increases owing to the larger bending deformation of the wing. At the same time, the lift force along the wingspan direction decreases. Thus, the aircraft should increase the angle of attack to provide sufficient lift force and ensure that the aircraft flies flat. To guarantee that the resultant force along the vertical axis is zero, the balancing thrust of the propulsion system should be increased accordingly. Simultaneously, based on the calculation results in Figure 6, the trim deflection angle of the elevator deflection increases with increasing payload mass. In comparison with highly flexible aircraft, the state variables and the trim input of the rigid aircraft vary with flat trend, and the thrust force is unchanged.

Utilizing the obtained trim states to linearize the model, the short-period and long-period modes with various payloads are obtained. Considering an element number of 24, the linearized matrices are $A \in R^{155\times155}$, $B \in R^{155\times2}$, $C \in R^{155\times155}$, and $D \in R^{155\times2}$, where I is the identity matrix. Based on the linearized model, the eigenvalues of the system are presented in Figures 8. The analysis shows that most of the eigenvalues of highly flexible aircraft are distributed near the origin; hence, the motion is mainly characterized by the long-period mode characteristics. The model does not show the short-period mode, which is a longitudinal mode exhibiting a higher frequency and damping ratio than the phugoid. Instead, there is a longitudinal pair of stable, real eigenvalues. This behavior was also seen in literature [52].

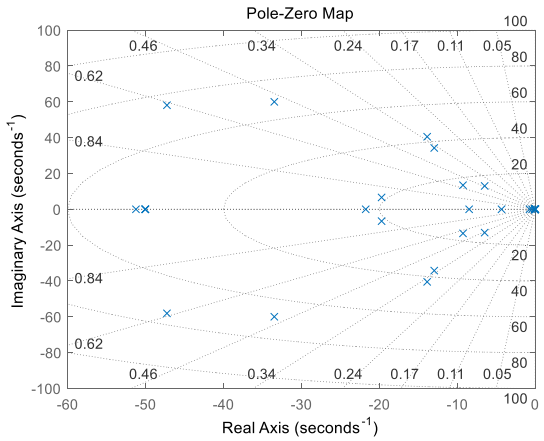

FIGURE 8. The eigenvalues near the origin of axes.

Increasing the payload from 0 to 227 kg, the eigenvalues of the long-period mode of highly flexible aircraft are compared with those of rigid aircraft, which are provided in Table 3 and Figure 9.

Table 3 and Figure 9 show that by increasing the payload mass, the eigenvalues of the long-period mode gradually approach the imaginary axis. When the payload is heavier than 28 kg, the eigenvalue passes through the imaginary

TABLE 3. The eigenvalues of long-period mode with a varying payload mass.

Payload (kg)	Rigid aircraft	Highly flexible aircraft
0	-0.0621±0.2740i	-0.0606±0.2444i
20	-0.0621±0.2834i	-0.0222±0.2704i
28	-0.0621±0.2872i	-0.0070±0.2795i
50	-0.0620±0.2966i	0.0355±0.3021i
80	-0.0619±0.3111i	0.0966±0.3282i
110	-0.0617±0.3245i	0.1644±0.3501i
140	-0.0614±0.3390i	0.2429±0.3691i
170	-0.0611±0.3503i	0.3366±0.3879i
200	-0.0608±0.3634i	0.4457±0.4103i
227	-0.0604±0.3746i	0.5544±0.4285i

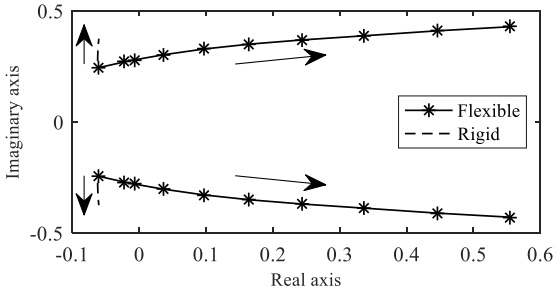

FIGURE 9. The eigenvalues of long-period mode with a varying payload mass.

axis into the unstable right half-plane. At this time, the aircraft mode becomes unstable, indicating that the payload mass directly affects the dynamic stability of highly flexible aircraft; however, the long-period mode of rigid aircraft is always in a stable region.

Thus, the long-period mode of flexible aircraft possesses an unstable characteristic root, causing some difficulties in the closed-loop control design of the system. The accessibility of the closed-loop system is affected by control saturation and other constraints. In this paper, the positive characteristic roots are obtained by solving the high-dimensional model of highly flexible aircraft. Moreover, by changing the payload, the aircraft possesses unstable modes over a long period. Hence, the effect of flexibility on the controllable performance of the aircraft system is investigated along with the control saturation constraints.

III. NULL CONTROLLABLE REGION

The nonlinear dynamic model of highly flexible aircraft has strong coupling characteristics, which makes it difficult to study the stable boundary. In addition, the model of highly flexible aircraft has higher dimensionality and more unstable eigenvalues than the rigid-body system. Due to the high dimensionality of aircraft, the calculation of the stable boundary requires a great deal of computation based on invariant sets. If the system is not controllable and observable, the stable boundary may have no feasible solution. Many studies have suggested that the system characteristics of highly flexible aircraft can be analyzed through linearization models [5-6,11]. Hence, this paper measures the convergence region of the aircraft with the stability radius and determines the closed-loop stability boundary under control saturation and state constraints in terms of the linearized model of highly flexible aircraft.

The dynamic model of highly flexible aircraft is explained in the form of Jacobian linearization:

$$\dot{x}(t) = Ax(t) + Bu(t) \tag{4}$$

where $x \in R^n$ represents system state. $u \in R^m$ shows the control input with saturation constraints satisfying the condition. It is assumed that the input saturation constraint has a symmetric form $|\bar{u}_-| = |\bar{u}_+| = \bar{u}$. Moreover, for $\forall t > 0$, the control input satisfies the condition:

$$u_i^2(t) < \bar{u}_i^2, \quad i = 1, 2, \cdots, m \tag{5}$$

Through the scale transformation of the B matrix, the amplitude limit of the input signal is limited $\bar{u} = 1$.

Definition 1: $\forall t > 0$, the actuator of the system meets the condition (5). If the control signal $u(t)$ always satisfies the above circumstances, it is termed admissible control at the saturated constraint, and the set of all the admissible control signals is represented as U_a [35].

Definition 2: For the primary state x_0, if there exit a finite time $T > 0$ and an admissible control signal $u(t) \in U_a$, let the state trajectory satisfies $x(T, x_0, u) = 0$, then the x_0 is known as the null controllable state. The set of all null controllable states is termed the null controllable region denoted as C [35].

For the null controllable region C [35], there exist several propositions such that:

1) If the matrix A is semi-stable, then $C = R^n$;
2) If the matrix A is anti-stable, then C is a convex open set including the origin;
3) If

$$A = \begin{bmatrix} A_1 & 0 \\ 0 & A_2 \end{bmatrix},$$

with $A_1 \in R^{n_1 \times n_1}$ anti-stable and $A_2 \in R^{n_2 \times n_2}$ semi-stable, and B is partitioned accordingly as

$$B = \begin{bmatrix} B_1 \\ B_2 \end{bmatrix},$$

then,

$$C = C_1 \times R^{n_2 \times n_2},$$

where C_1 is the null controllable region of the anti-stable system

$$\dot{x}_1 = A_1 x_1 + B_1 u.$$

4) If $B = [b_1, \cdot, b_m]$, and the null controllable region of the subsystem $\dot{x} = Ax + b_i u_i$ is C_i, then the null controllable region of the system is:

$$C = \sum_{i=1}^{m} C_i = \{x_1 + \cdots + x_m : x_i \in C_i\} \tag{6}$$

Considering the above schemes, the high-order multivariable system can be simplified to a single input anti-stable system ($A > 0$). The null controllable region of a single input linear system is provided by an integral form of admissible control stated as [53]

$$\bar{C} = \left\{ x | x = \int_0^\infty e^{-A\tau} B u(\tau) d\tau, u \in U_a \right\} \quad (7)$$

where $\bar{C}$ is the closure of C, and ∂C is the boundary of the null controllable region C.

Definition 3: For the dynamic system (4), the radius stability is defined as the least 2-norm of the points at the null controllable region boundary ∂C:

$$D_c = \min \{ \|x\|_2 | x \in \partial C \} \quad (8)$$

For the radius stability, there is a property exist:

$$\forall \|x_0\|_2 < D_c, \quad x_0 \in C$$

Hence, the null controllable region of the system is obtained by the above properties and definitions, and the range of the null controllable region of the system can be determined through the stability radius.

A. STABILITY RADIUS OF 1ST ORDER SYSTEM

Consider a 1st order unstable system with control saturation and the equation of

$$\dot{x}(t) = ax(t) + bu(t), |u(t)| \leq 1 \quad (9)$$

where $a > 0$. Assuming that the system control is symmetry constraint. Without loss of generality, assume that $b > 0$.

Definition 4: For the 1st order system (9) and the initial state x_0, considering the control signal $u(t) = -1$, the state trajectory is explained as the lower bound trajectory, given as $\underline{x}(t, x_0)$. Following the same process with the condition of the control signal $u(t) = 1$, the state trajectory is explained as the upper bound trajectory of x_0, given as $\bar{x}(t, x_0)$.

Under the action of any admissible control signal $u \in U_a$, the state trajectory meets the following circumstances:

$$\underline{x}(t, x_0) \leq x(t, x_0, u) \leq \bar{x}(t, x_0) \quad (10)$$

There is a conclusion based on literature [29]. Regarding the first-order system (9) with the limitation of input saturation, keep initial value $x_0 > 0$ ($x_0 < 0$), when the time $T > 0$ does not exist for satisfying $\underline{x}(T, x_0) \leq 0 (\bar{x}(T, x_0) \geq 0)$, then the system is diverging. The null controllable region is restricted by the value of the unstable pole λ. For a 1st order system, there is a relation that the system pole $\lambda = a$. Then, the system stability radius is $D_C = b/a$.

B. STABILITY RADIUS OF 2ND ORDER SYSTEM

In the case of the second-order system and where the unstable pole is a pair of complex conjugate numbers, then the basic form of the system is written as

$$\begin{bmatrix} \dot{x}_1 \\ \dot{x}_2 \end{bmatrix} = A \begin{bmatrix} \dot{x}_1 \\ \dot{x}_2 \end{bmatrix} + Bu = \begin{bmatrix} \sigma & -\omega \\ \omega & \sigma \end{bmatrix} \begin{bmatrix} \dot{x}_1 \\ \dot{x}_2 \end{bmatrix} + \begin{bmatrix} b_1 \\ b_2 \end{bmatrix} u \quad (11)$$

When the system pole includes a pair of complex conjugate numbers, it has periodical behavior. To qualitatively analyze the 2nd order periodic equation, the basic way is to investigate the solution after one period with any initial value. Thus, the Poincare map is utilized by

$$P(x_0) = x(T, x_0) : R^2 \to R^2 \quad (12)$$

If the period is $T = 2\pi/\omega$ and the initial phase is ϕ_0, then the periodic limit control is obtained as

$$u_T(t, \phi_0) = sign[\sin(\omega t + \phi_0)] \quad (13)$$

Theorem 1: When the system takes a fixed point of Poincare map as the initial value, the system trajectory under the action of periodic limit control (13) is a closed orbit, which is the boundary ∂C of the system's null controllable region.

Consider that the initial phase of the periodic limit control signal is 0 and the period is $T = 2\pi/\omega$. Then, the Poincare map of the initial state x_0 is

$$P(x_0) = e^{AT} x_0 + (e^{A\frac{T}{2}} - I) A^{-1} B \quad (14)$$

where A represents the state matrix and B shows the control matrix of the system. The fixed point of the Poincare map is obtained by

$$x_p = \frac{(1 + e^{\pi\sigma/\omega})}{(1 - e^{\pi\sigma/\omega})} A^{-1} B \quad (15)$$

The closure of the periodic system is symmetric about the origin. Hence, the null controllable region can be investigated by solving the trajectory of the fixed point of the Poincare map in the half period. The fixed point of Poincare map (x_p) is provided as

$$x(t, x_p) = [e^{At} \frac{2}{1 - e^{\pi\sigma/\omega}} - I] A^{-1} B, t \in [0, T/2] \quad (16)$$

Thus, the stability radius of the 2nd order unstable system is explained by calculating the minimum 2-norm of Poincare mapping fixed point trajectory as

$$D_c = \min_{t \in [0, T/2]} ||x(t, x_p)||_2 \quad (17)$$

C. STABILITY RADIUS OF HIGHLY FLEXIBLE AIRCRAFT

The dynamic model of highly flexible aircraft based on the finite element method includes the high dimensions making is difficult to analyze the system controllability. Hence, the general low-order system stability radius analysis strategy is not applicable. In this paper, the null controllable region of highly flexible aircraft is studied based on the eigenvectors and eigenvalues.

To compare the dynamic responses of different element numbers, numerical simulations of literature [47] show that the 47 states could be used to represent the dynamics of highly flexible aircraft. When the basic number of finite elements is 6, then the dynamic system dimension is $n = 47$. Consider an n order state matrix A with stable characteristic roots $w_i, i = 1, \cdots m$, unstable characteristic roots, $q_i, 1, \cdots, k$,

and $k + m = n$. The arbitrary state of the system is decomposed into the complex field with the geometric multiplicity of all the eigenvalues of the matrix A equal to algebraic multiplicity.

$$x = \sum_{i=1}^{n} k_i \lambda_i \tag{18}$$

where $x \in R^{47}$ represents the system state, $\lambda_i \in C^{47}$ shows the eigenvector equivalent to the eigenvalues $p_i = \sigma_i + i\omega_i$ respectively, and $k_i \in$ C is component of the system state on the eigenvector λ_i. For the complex conjugate, the conjugate relationship is satisfied by eigenvalues and their corresponding eigenvectors, hence, the system states are in the real linear space.

Based on the literature [29], it is indicated that for the $n \times n$ matrix A, the right eigenvectors are orthogonal to left eigenvectors equivalent to various eigenvalues [28], as

$$\eta_j^H \cdot \lambda_i = 0, \quad i \neq j \tag{19}$$

where η_j^H represents the conjugate transpose of the vector η_j.

By using the component form of state, the dynamic system is transformed into a differential equation of the component of state along the eigenvector. Therefore, the differential equation of highly flexible aircraft can be written as

$$\sum_{i}^{n} \dot{k}_i \lambda_i = \sum_{i}^{n} \dot{k}_i A \lambda_i + Bu = \sum_{i}^{n} \dot{k}_i p_i \lambda_i + Bu \tag{20}$$

Pre-multiplying equation (20) by the left eigenvector η_j^H of the unstable eigenvalue, the differential equation of the component k_i of system state along λ_j is found by equation (19), as

$$\dot{k}_j = p_j k_j + \frac{\eta_j^H B}{\eta_j^H \lambda_j} u \tag{21}$$

Hence, by solving the component k_j, the radius stability issue is simplified. For the real eigenvalue $q_j \in R, k_j \in R$, therefore, the system (21) is a 1st order system. For the complex eigenvalue $q_j = \sigma_j + i\omega_j, \sigma_j, \omega_j \in R, k_j = x_j + iy_j, x_j, y_j \in R$, the system (21) is provided as a 2nd order system in real number field as

$$\begin{bmatrix} \dot{x}_j \\ \dot{y}_j \end{bmatrix} = \begin{bmatrix} \sigma_j & -\omega_j \\ \omega_j & \sigma_j \end{bmatrix} \begin{bmatrix} x_j \\ y_j \end{bmatrix} + \begin{bmatrix} b_x \\ b_y \end{bmatrix} u \tag{22}$$

where, b_x, b_y denote the real and imaginary sections of the control input coefficient in the system (21), respectively and expressed as

$$b_x + \mathrm{i} b_y = \frac{\eta_j^T B}{\eta_j^T \lambda_j} \tag{23}$$

The stability of highly flexible aircraft is analyzed from the component k_j of states and the eigenvectors, therefore, the high-order system is translated into simpler 1st or 2nd order anti-stable mode. For the high-order system, set the radius of convergence of the ith unstable mode D_{C_i}. Hence, the stability radius of the full system is not larger than each sub-model's stability radiuses.

$$D_c \leq \min_i \left\{ D_{c,i} \right\} \tag{24}$$

Therefore, the stability radius of highly flexible aircraft under the control input saturation constraints is obtained.

IV. NUMERICAL SIMULATIONS

When the control system design is not taken into account, the closed-loop stability boundary of highly flexible aircraft is associated only with the open-loop features of the dynamic system and the control signal saturation constraints. If the specific form of the closed-loop feedback controller is defined, then the closed-loop stability boundary of highly flexible aircraft will shrink. After adding the state constraint of the aircraft, the null controllable region will further decrease. In this paper, two control inputs are considered for highly flexible aircraft, namely, elevator deflection and engine thrust. In this section, elevator deflection is taken as an example, considering the saturation constraint of elevator deflection to study the influence of the control constraints on the null controllable region of highly flexible aircraft. By applying the method of Newmark α, setting the step size in the simulation as $\Delta t = 0.025s$ and limiting the spectral radius to $\rho_{\infty_2} = 0.99$, numerical simulations are performed based on the linear model.

A. STABILITY BOUNDARY OF HIGHLY FLEXIBLE AIRCRAFT WITH CONTROL SATURATION $|\delta_e| \leq 10°$

By setting the highly flexible aircraft to fly at a speed of 12.58 m/s at sea level with a 0 kg payload, the stability boundary is investigated in terms of the equilibrium state. To increase the stability of the system, a feedback controller is designed based on a linear-quadratic regulator (LQR). The stability of the closed-loop control system is studied when the initial state deviates from the equilibrium state. Then, it is analyzed whether the stability augmentation system (SAS) can achieve the controllability of the whole system under state constraints and saturation constraints.

Designing LQR control parameters as $Q = diag(\lambda_1, \lambda_2, \lambda_3, \lambda_4, \lambda_5, \lambda_6, \cdots, \lambda_{26}, \lambda_{27}, \cdots, \lambda_{47})$, where $\lambda_1 = \lambda_2 = 10, \lambda_3 = \lambda_4 = \lambda_5 = 1, \lambda_6 = \cdots = \lambda_{26} = 0.2, \lambda_{27} = \cdots = \lambda_{47} = 0.01, R = diag(1, 5)$, the feedback control matrix $K_{2\times 47}$ is obtained as

$$\begin{aligned} K = \Big[& -1.8495 \ -4.8728 \ \ 9.9486 \ \ 57.6156 \\ & \ \ 0.0993 \ \ \ 0.0208 \ -0.0369 \ -0.2349 \\ & \cdots \ 0.9881 \ \ 0.0082 \ \ \ 0.0337 \ -0.0060 \\ & \cdots \ 0.0689 \ -0.0002 \ -0.0027 \ \ 0.0007 \\ & \cdots -910.8005 \ 189.5156 \ -36.8356 \ -0.2829 \\ & \cdots \ \ \ 0.0052 \ \ \ -0.0242 \ \ 0.0804 \ \ \ 0.0001 \\ & \cdots -0.0814 \ -8.0881 \ 0.0004 \ \ 2.9873 \\ & \cdots -0.0141 \ \ 0.0002 \ \ 0.0000 \ -0.0117 \\ & \cdots \ \ 0.0028 \ \ \ 0.2836 \ \ -0.0835 \ \ 8.0933 \\ & \cdots -0.0000 \ -0.0000 \ -0.0141 \ -0.0002 \end{aligned}$$

$$\begin{bmatrix} \cdots 910.8103 & 189.5135 & 36.7728 & -0.0081 \\ \cdots -0.0052 & -0.0242 & -0.0804 & -0.0001 \\ \cdots 0.0295 & -0.0077 & 0.1340 & 0.7552 \\ \cdots -0.0027 & -0.0008 & 0.0001 & 0.0005 \\ \cdots 1.3590 & 0.0661 & 0.7096 & 0.3370 \\ \cdots 0.0006 & 0.0001 & 0.0006 & -0.0000 \\ \cdots -0.0066 & 0.2737 & -0.2254 & -0.0005 \\ \cdots -0.0000 & 0.0007 & 0.0001 & 0.0000 \\ \cdots 0.2773 & 0.0002 & 0.0065 & 0.2735 \\ \cdots 0.0008 & 0.0000 & 0.0000 & 0.0005 \\ \cdots 0.2250 & -0.0662 & 0.7099 & -0.3367 \\ \cdots -0.0000 & -0.0000 & 0.0006 & 0.0000 \\ \cdots -0.1340 & 0.7552 & -1.3590 & \\ \cdots -0.0000 & 0.0005 & -0.0006 & \end{bmatrix} \quad (25)$$

In this paper, the saturation constraint of the elevator deflection of highly flexible aircraft is considered. In general, a relaxed constraint range of elevator deflection is more beneficial for designing feedback control to achieve the control objectives and system stability. To better study the effect of the saturation constraint on the null controllable region of the system, this section considerably reduces the saturation constraint of elevator deflection to obtain the strictly convergent null controllable region. The trajectory of the initial state from this region will also tend to be stable over a finite time when the saturation constraint is relaxed.

Let the saturation constraint of the elevator deflection be $|\delta_e| \leq 10°$. Considering the airspeed and pitch angle as objects reflecting the long-period mode, the influence of the amplitude of the two state variables deviating from the equilibrium state on the system's controllability is investigated. Based on the technique for determining the stability boundary, the convergence region of the system under the stability augmentation system (23) in the equilibrium state is obtained, as shown in Figure 10.

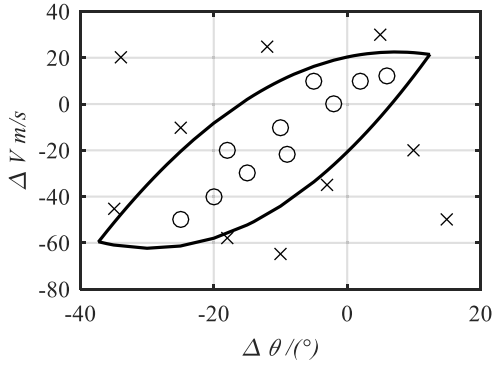

FIGURE 10. The convergence region of the system under saturation constraint of $|\delta_e| \leq 10°$.

Figure 10 shows the null controllable region of the airspeed and increased pitch angle under the saturation constraint $|\delta_e| \leq 10°$. The area contained in the curve is the convergence region. Based on the initial states (such as the circles in Figure 10) in this region, the equilibrium state will be created in the system motion followed by the stability augmentation system effect in a finite time. The initial states from outside the region (such as the crosses in Figure 10) tend to diverge after a certain period.

An actual highly flexible aircraft includes restrictions on the flight states in addition to constraints on the elevator deflection. Therefore, the null controllable region of the real system will shrink further. Considering the actual state constraints and performance requirements, the main parameters, such as the angle of attack, speed and thrust, are chosen for investigation. For this paper, the stall angle of attack is set to 15°, which is close to those obtained in reference [52] ($\alpha_{stall} = 15°$) and reference [51] ($\alpha_{stall} = 14°$). In addition, the stall speed is calculated as 6 m/s based on the stall angle of attack. Finally, the constraints of the highly flexible aircraft are defined as follows:

$$\begin{aligned} 6m/s &< V \\ -10° &< \alpha < 15° \\ 0 &< T < 100N \end{aligned} \quad (26)$$

The equilibrium states of the aircraft are considered to be

$$\begin{aligned} V_0 &= 12.58m/s \quad \alpha_0 = 2.8° \; \theta_0 = 2.8° \\ \delta_{e0} &= 4.9° \quad T_0 = 36.6N \end{aligned} \quad (27)$$

After transformation, the constraints on the control inputs and the states of highly flexible aircraft can be obtained as

$$\begin{aligned} -6.58m/s &< \Delta V \\ -12.8° &\leq \Delta\alpha \leq 12.2° \\ -14.9° &\leq \Delta\delta_e \leq 5.1° \\ -36.6N &< \Delta T \leq 63.4N \end{aligned} \quad (28)$$

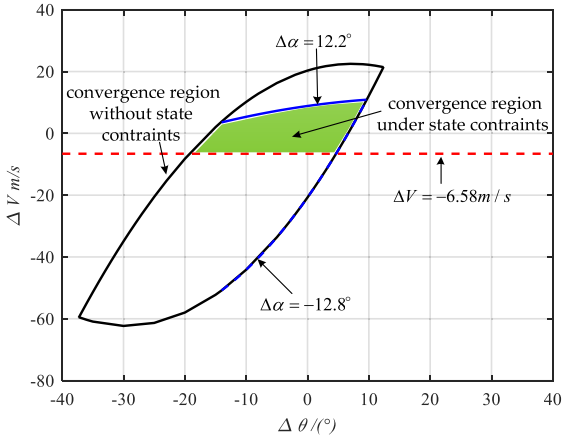

FIGURE 11. The convergence region under state constraints.

Based on the system convergence domain estimation and stability radius method and considering the constraint of equation (28), the closed-loop stability boundary under the constraint conditions is obtained by solving the LMI constraint equations (Figure 11). The colored region in Figure 11 is the closed-loop stable convergence domain of the system under the comprehensive consideration of the

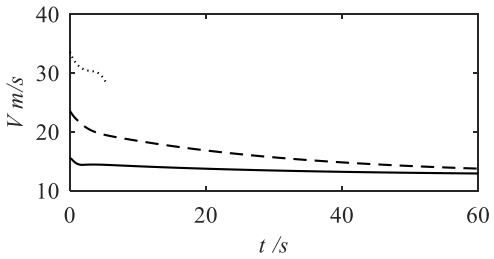

(a) Velocity

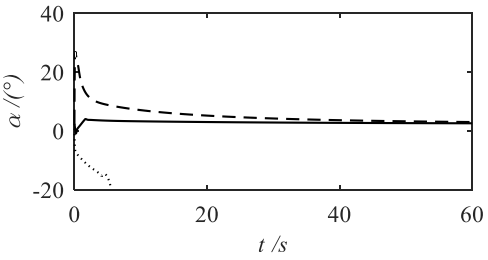

(b) Angle of attack

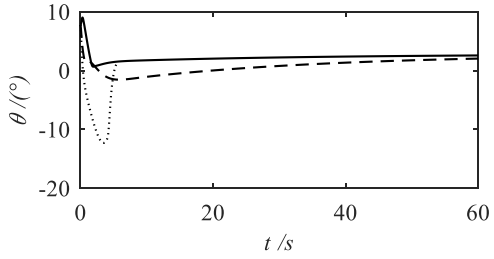

(c) Pitch angle

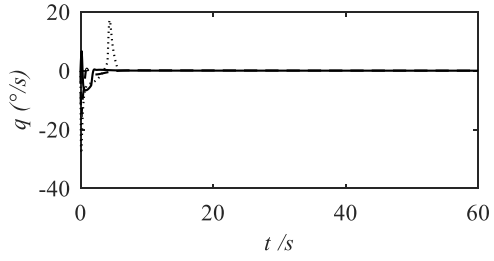

(d) Pitching rate

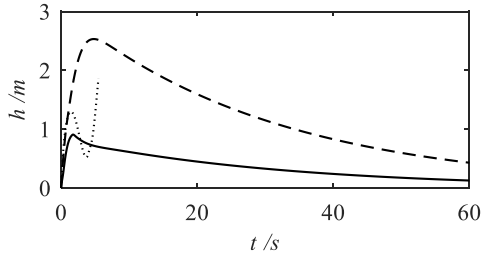

(e) Altitude

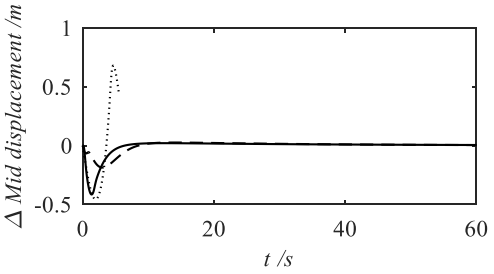

(f) Wing root bending displacement

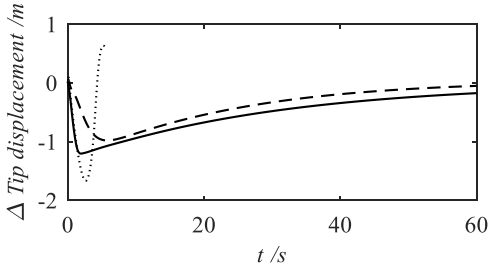

(g) Wing tip bending displacement

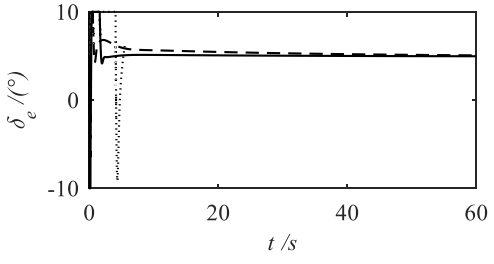

(h) Elevator deflection angle

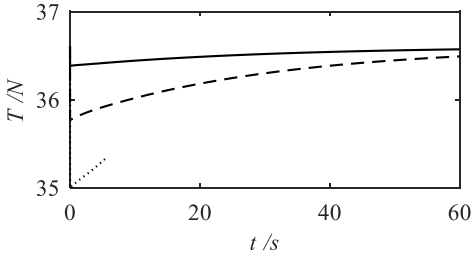

(i) Thrust per motor

FIGURE 12. Response of aircraft under saturation constraints and state constraints. —— $\Delta\theta = 5°, \Delta V = 3m/s$; - - - - - $\Delta\theta = 5°, \Delta V = 11m/s$; ..... $\Delta\theta = 5°, \Delta V = 21m/s$.

system thrust constraint and the state constraints (28). The dashed line is the lower bound of the closed-loop stable boundary equivalent to each state constraint of the highly flexible aircraft, and the solid line represents the upper bound of the closed-loop stable boundary corresponding to each state constraint. For the initial values of the velocity and pitch angle limited to the colored domain, the transient response of highly flexible aircraft tends to stabilize in a finite time. In contrast, for an initial value outside the green domain, the transient response tends to diverge under the stability augmentation system.

Based on Figure 11, the colored region is the stability boundary of the closed-loop system. The convergence region under the state constraints and input constraints will shrink substantially considering a highly flexible aircraft system with practical significance. To verify this closed-loop stability region, this section chooses the initial states $\Delta\theta = 5°$, $\Delta V = 3m/s$, $\Delta\theta = 5°$, $\Delta V = 11m/s$ and $\Delta\theta = 5°$, $\Delta V = 21m/s$. The initial value of $\Delta V = 3m/s$ is limited to the convergence region, and the initial value of $\Delta V = 11m/s$ exceeds the case with a constraint of $\Delta\alpha = 12.2°$. When the initial value is $\Delta V = 21m/s$, the case with the constraints of unstable eigenvalues and inputs will be active. Then, the numerical simulations operate on the linear model. The output responses under the stability augmentation system are shown in Figure 12.

Figure 12 shows the motion responses of the highly flexible aircraft in three initial states. Figure 12 (h) shows the change in the elevator deflection angle under the saturation constraint. The flight state of the highly flexible aircraft is stable, and all the state responses meet the constraint requirements when the initial state is $\Delta\theta = 5°$, $\Delta V = 3m/s$. The aircraft can reach the equilibrium state under the action of the controller when the initial state is $\Delta\theta = 5°$, $\Delta V = 11m/s$. However, the angle of attack exceeds the upper bound during the motion and no longer meets the performance requirements. When the initial state is $\Delta\theta = 5°$, $\Delta V = 21m/s$, the region diverges after a certain period. Then, the controller can no longer ensure the stability of the system under the state constraints and saturation constraints.

In conclusion, the simulations of Figure 12 confirm the effectiveness of the obtained closed-loop stability boundary in terms of the proposed technique. The influence of the initial variables, such as the pitch angle and velocity, on the null controllability region of the aircraft system is shown. Constraint requirements for the initial state increments of highly flexible aircraft are proposed.

B. STABILITY BOUNDARY OF HIGHLY FLEXIBLE AIRCRAFT WITH CONTROL SATURATION $|\delta_e| \leq 20°$

Given that the saturation constraint of the elevator $|\delta_e| \leq 10°$ is strictly conservative, in this section, the saturation constraint is set to 20° to further study the effect of the relaxed elevator deflection constraint on the convergence region of highly flexible aircraft. When the state constraints and other control input constraints are unchanged, the

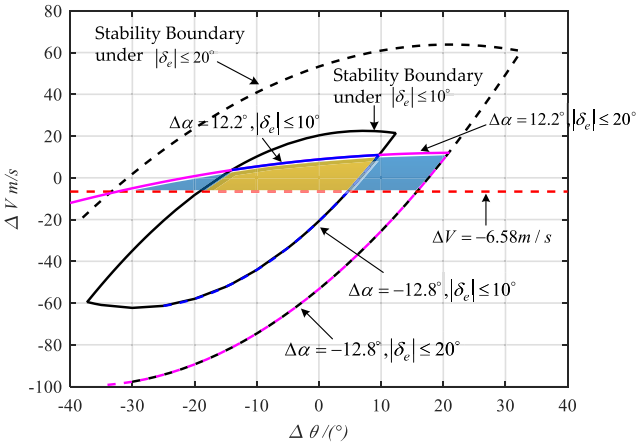

FIGURE 13. The comparison of convergence domains between $|\delta_e| \leq 10°$ and $|\delta_e| \leq 20°$.

closed-loop stable convergence domain of the system is solved considering the LQR feedback control under the saturation constraint $|\delta_e| \leq 20°$. The comparison of the convergence domain between the constraint conditions $|\delta_e| \leq 10°$ and $|\delta_e| \leq 20°$ is provided in Figure 13.

In Figure 13, the black solid line represents the closed-loop stability boundary under the single constraint $|\delta_e| \leq 10°$, and the orange region is the strict convergence domain satisfying all constraint conditions under the constraint $|\delta_e| \leq 10°$. The black dashed line shows the convergence domain under the single saturation constraint $|\delta_e| \leq 20°$, and the blue region is the strict convergence domain meeting all constraint circumstances under the constraint $|\delta_e| \leq 20°$.

In Figure 13, the black solid line is the closed-loop stable boundary under the constraint $|\delta_e| \leq 10°$, and the black dashed line in the figure is the upper part of the closed-loop stability boundary under the constraint $|\delta_e| \leq 20°$. When the saturation constraint of the elevator is relaxed to $|\delta_e| \leq 20°$, the null controllable region of the system significantly increases, and the closed-loop convergence domain completely includes the domain under the constraint $|\delta_e| \leq 10°$. Considering state constraints such as airspeed and angle of attack and control input constraints such as elevator deflection and engine thrust, the closed-loop stable convergence domain of highly flexible aircraft shrinks substantially. Figure 13 indicates that the orange region of $|\delta_e| \leq 10°$ is completely surrounded by the blue region of $|\delta_e| \leq 20°$. The constraint condition of the angle of attack imposes a higher requirement on the increasing speed of highly flexible aircraft and defines the upper bound of the speed increment in the equilibrium state. Simultaneously, it is observed that when the saturation constraint on the elevator is relaxed, the lower bound of the speed increment is broadened from the blue dashed line to the pink dashed line. For both cases of $|\delta_e| \leq 10°$ and $|\delta_e| \leq 20°$, the lower bound of the null controllable regions is confirmed by the stall speed.

To verify the closed-loop stability region of $|\delta_e| \leq 10°$ and $|\delta_e| \leq 20°$, this section chooses the initial state

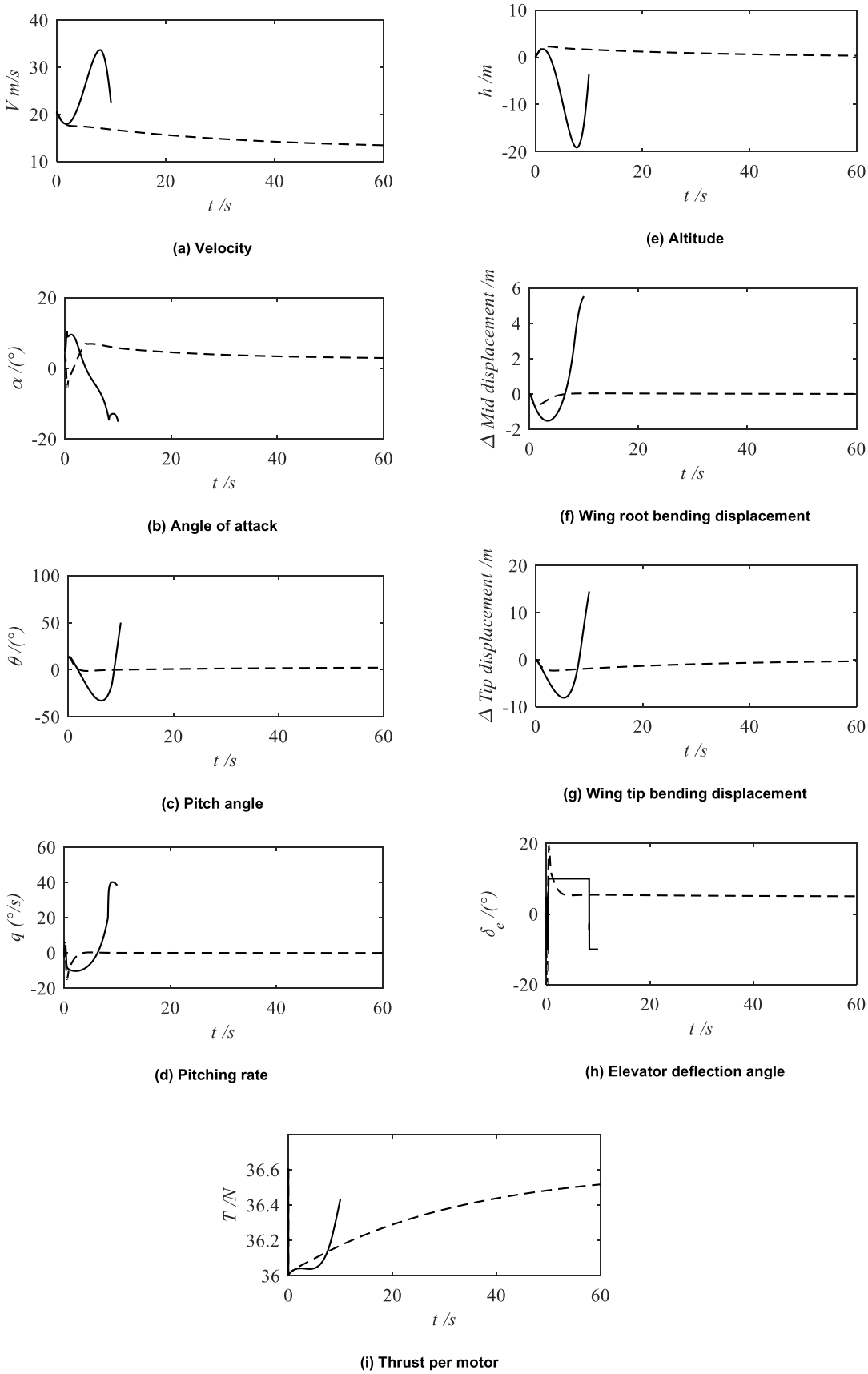

(a) Velocity

(e) Altitude

(b) Angle of attack

(f) Wing root bending displacement

(c) Pitch angle

(g) Wing tip bending displacement

(d) Pitching rate

(h) Elevator deflection angle

(i) Thrust per motor

FIGURE 14. Comparison of response between $|\delta_e| \leq 10°$ and $|\delta_e| \leq 20°$. —— $|\delta_e| \leq 10°$; - - - - - $|\delta_e| \leq 20°$.

$\Delta\theta = 10°, \Delta V = 8m/s$. The simulation responses are provided in Figure 14. According to the simulation figures, when the saturation constraint of the elevator deflection is $|\delta_e| \leq 20°$, the aircraft state can be guaranteed to converge to the equilibrium state, and the performance constraints are met by all the states and the control trajectory in the whole motion procedure, which is consistent with the results in Figure 13. Focusing on the saturation constraint $|\delta_e| \leq 10°$, the motion process of the aircraft gradually diverges, indicating that the constraints on the actuator greatly influence the controllability of the system.

When the actuator dynamics are considered, the saturation constraint may be defined for the state derivative (rate limit). Research on this case is very important. To analyze the constraint for the state derivative, the stability boundary has been studied under varying input rates. The related research process is based on literature [54]. The research shows that the elevator rate can directly affect the controllability of highly flexible aircraft. When the rate of change of the elevator is too great, the aircraft system may not be able to stabilize in a finite time.

C. STABILITY BOUNDARY INFLUENCED BY DAMPING

Unlike conventional aircraft, a structural flexibility of $|\delta_e| \leq 10°$ brings unique features to highly flexible aircraft, affecting system controllability and performance. It is essential to theoretically analyze the influence of flexible parameters on the stability boundary [6]. In this section, the damping factor is chosen as the research object to analyze its effect on the stability boundary of highly flexible aircraft. The damping factor is the coefficient between the damping and stiffness matrix in the equation $C = cK$, where C, c and K are the damping matrix, damping factor and stiffness matrix, respectively. Considering that Equation (28), the constraint condition, remains unchanged and selecting damping factors of $c = 0.02$ and $c = 0.04$, the closed-loop stable convergence domain of the system is determined under the elevator constraint $|\delta_e| \leq 10°$ based on the stability augmentation system in this section. The comparison of the convergence domains for $c = 0.02$ and $c = 0.04$ is provided in Figure 15.

In Figure 15, the black solid line represents the closed-loop stability boundary corresponding to the damping factor $c = 0.02$, and the green region is the strict convergence domain that satisfies all constraint circumstances with the damping factor $c = 0.02$. The black dashed line shows the convergence domain equivalent to each state constraint condition with the damping factor $c = 0.04$, and the orange region is the strict convergence domain meeting all constraint circumstances with the damping factor $c = 0.04$.

The black line represents the stability boundary of the system corresponding to the damping factors $c = 0.02$ and $c = 0.04$ without considering the state constraints. The boundary is related only to the zero-pole position, the control input saturation constraint, and the LQR control design. Therefore, the closed-loop stable boundary reflects the essential characteristics of the system. Compared with $c = 0.02$,

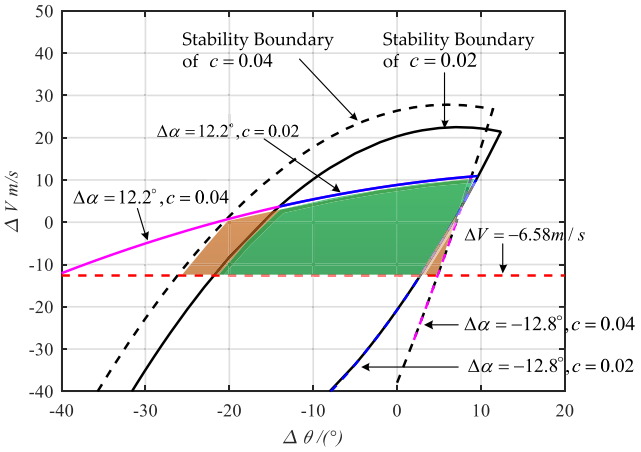

FIGURE 15. The comparison of stability boundary between $c = 0.02$ and $c = 0.04$.

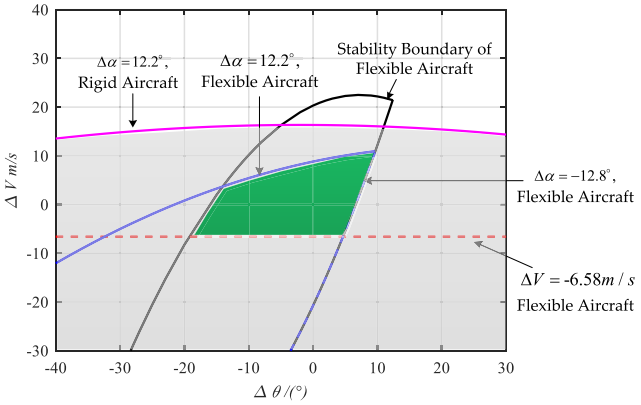

FIGURE 16. The comparison of stability boundary between rigid aircraft and flexible aircraft.

the null controllable region of $c = 0.04$ is much larger. The green null controllable region of $c = 0.02$ is completely surrounded by the orange region of $c = 0.04$. This shows that when the damping factor of a highly flexible aircraft is smaller, there will be higher constraint requirements on the velocity and pitch angle. If the allowable increment of the velocity and pitch angle exceeds the controllable range, the motion process of the aircraft will tend to diverge.

Figure 15 shows that considering the actual state constraints of highly flexible aircraft, the stability boundary of the damping factor $c = 0.02$ is smaller than the boundary of the damping factor $c = 0.04$. It is indicated that the convergence domain will be reduced when the structural flexibility of the aircraft is more obvious, bringing more stringent requirements for the aircraft state deviation and greater difficulty to the control system design.

D. COMPARISON OF STABILITY BOUNDARY BETWEEN RIGID AND FLEXIBLE AIRCRAFT

To further compare the stability boundaries of rigid and flexible aircraft, the rigid aircraft model is obtained by eliminating the flexibility from the highly flexible aircraft model in this paper, and the stable boundary is solved for both aircraft.

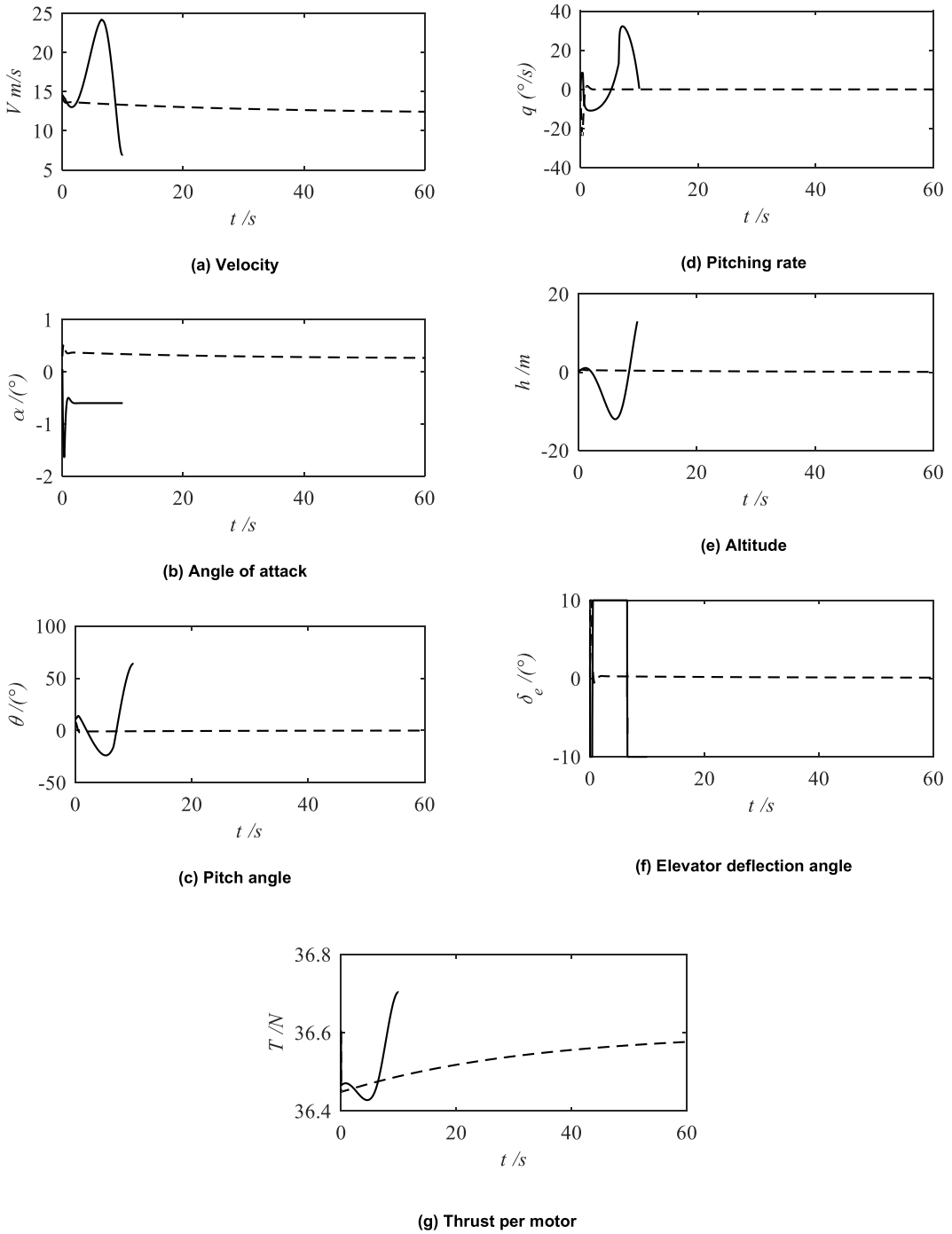

FIGURE 17. Comparison of response between rigid aircraft and flexible aircraft. —— Highly flexible aircraft; - - - - - Rigid aircraft.

The state constraints and control input constraints remain unaffected. The closed-loop stable convergence domain of the system is calculated considering the LQR feedback control in this paper. The LQR gains for the rigid aircraft are obtained directly by a partition of the gain matrix of equation (25). With the first 5 orders of equation (25), which reflect the rigid motion, the dimension of the control matrix $K_{rigid} \in R^{2\times5}$ is chosen. A comparison of the stability boundaries of the rigid aircraft and highly flexible aircraft is shown in Figure 16.

In Figure 16, the green area is the strict convergence domain satisfying all the constraints of the highly flexible aircraft. The gray region is the strict convergence domain meeting all the constraints of the rigid aircraft. According to the calculation results, the convergence domain of the rigid aircraft is much wider than that of the highly flexible aircraft. Without considering constraints such as state constraints, the system convergence domain completely contains the closed-loop stability region of the highly flexible aircraft.

Therefore, the system convergence domain of the rigid aircraft is not shown in Figure 16. According to Table 3, the rigid aircraft is open-loop stable in the long-period mode for all payload values. Therefore, the convergence domain of the rigid aircraft without state constraints is infinite. When performance constraints such as system states are taken into account, the convergence domains of the rigid-body aircraft and highly flexible aircraft are shown in the color rendering region in Figure 16. For the rigid aircraft, the constraint on the angle of attack has a specific constraint for the speed and pitch angle. After considering the state constraints, the overall stability boundary of the rigid aircraft still completely contains the null controllable region of the highly flexible aircraft.

To further verify the system convergence domain of the highly flexible aircraft and rigid body aircraft, simulations are performed on the two aircraft with the initial state $\Delta\theta = 8°, \Delta V = 2m/s$, and the corresponding response curves are obtained as shown in Figure 17. According to the simulation diagrams, the response curves of the rigid body aircraft are flat and can converge to the equilibrium state. Moreover, the states and control trajectories satisfy all constraints in the whole motion process, which is consistent with the results in Figure 16. The motion process gradually diverges for the highly flexible aircraft. The flexibility influences the null controllable region of the system, negatively impacting the controllability of the highly flexible aircraft.

The thrust constraint has an important effect on the stability boundaries of the highly flexible aircraft. The closed-loop stability boundary under the constraint conditions is obtained by solving the LMI constraint equations, which include the thrust constraint. Under the LQR stability augmentation system, the numerical simulations in this paper do not reach the upper limit of 100 N. However, the thrust constraint is still an important factor in determining the stability boundary.

V. CONCLUSION

The dynamic system of highly flexible aircraft generates unstable modes by increasing the payload. Therefore, the controller is required to meet the closed-loop stability condition. Because of the amplitude saturation constraint in the control signal, the global stability of the system may not be ensured. In this paper, the open-loop characteristics of the system are analyzed, and a closed-loop system is designed based on an LQR. The stability boundary of the closed-loop system is quantitatively determined under the control signal saturation constraint. The theoretical analysis concludes that the stability boundary is defined by the position of the unstable pole in the system's open loop, the left eigenvector equivalent to the unstable pole, the B matrix of the equation, and the margin of control. Moreover, the stability radius is utilized to quantitatively analyze the local stability of the system.

Considering the fast time-varying dynamic features of highly flexible aircraft, the flexibility characteristics will certainly influence the control design of the aircraft. When saturation constraints exist in the actuator of the system, the stability boundary of the system will decrease further. Moreover, the degree of reduction is associated with the amplitude of the control input saturation constraint and the position of the unstable pole.

Ultimately, the effect of the controller saturation constraint on the closed-loop stability boundary is obtained quantitatively through numerical analysis. Given the dynamic features of a highly flexible aircraft with unstable poles and the limitation of the elevator deflection angle, the closed-loop stability boundary based on the LQR controller is investigated along with the state constraints. The effect of the damping factor on the null controllable region of the aircraft is analyzed, and the convergence regions of the highly flexible aircraft and rigid aircraft are compared. The simulations indicate that the convergence domain will be reduced as the structural flexibility of the aircraft increases, bringing more stringent requirements for the aircraft state deviation and greater difficulty for the control system design. In summary, our study can be utilized as a reference for the initial design and analysis of aircraft, which requires the evaluation of stability and controllability. Future interesting topics include the optimization design of dynamic modeling and integrated control for highly flexible aircraft [45], [55], [56].

ACKNOWLEDGMENT

The authors would like to thank the anonymous reviewers for their valuable comments and suggestions, which helped to improve the paper.

REFERENCES

[1] P. Qi, X. Zhao, Y. Wang, R. Palacios, and A. Wynn, "Aeroelastic and trajectory control of high altitude long endurance aircraft," *IEEE Trans. Aerosp. Electron. Syst.*, vol. 54, no. 6, pp. 2992–3003, Dec. 2018.

[2] C. Riso, F. G. Di Vincenzo, M. Ritter, C. E. S. Cesnik, and F. Mastroddi, "Nonlinear aeroelastic trim of very flexible aircraft described by detailed models," *J. Aircr.*, vol. 55, no. 6, pp. 2338–2346, Nov. 2018.

[3] N. Tsushima and W. Su, "A study on adaptive vibration control and energy conversion of highly flexible multifunctional wings," *Aerosp. Sci. Technol.*, vol. 79, pp. 297–309, Aug. 2018.

[4] W. Su, "Development of an aeroelastic formulation for deformable airfoils using orthogonal polynomials," *AIAA J.*, vol. 55, no. 8, pp. 2793–2807, Aug. 2017.

[5] Z. Wan and C. E. S. Cesnik, "Geometrically nonlinear aeroelastic scaling for very flexible aircraft," *AIAA J.*, vol. 52, no. 10, pp. 2251–2260, Oct. 2014.

[6] W. Su, "Dynamic aeroelastic response of highly flexible aircraft with wing camber deformations," in *Proc. 56th AIAA/ASME/ASCE/AHS/ASC Struct., Struct. Dyn. Mater. Conf.*, Kissimmee, FL, USA, Sep. 2020, Jan. 2015.

[7] C. Cesnik and W. Su, "Nonlinear aeroelastic modeling and analysis of fully flexible aircraft," in *Proc. 46th AIAA/ASME/ASCE/AHS/ASC Struct., Struct. Dyn. Mater. Conf.*, Austin, TX, USA, Apr. 2005, p. 2169.

[8] C. Riso, G. Riccardi, and F. Mastroddi, "Nonlinear aeroelastic modeling via conformal mapping and vortex method for a flat-plate airfoil in arbitrary motion," *J. Fluids Struct.*, vol. 62, pp. 230–251, Apr. 2016.

[9] R. Palacios and A. Cea, "Nonlinear modal condensation of large finite element models: Application of Hodges's intrinsic theory," *AIAA J.*, vol. 57, no. 10, pp. 4255–4268, Oct. 2019.

[10] W. Su and N. Tsushima, "Modeling of highly flexible multifunctional wings for energy harvesting," in *Proc. 56th AIAA/ASCE/AHS/ASC Struct., Struct. Dyn., Mater. Conf.*, Kissimmee, FL, USA, Jan. 2015, p. 444.

[11] N. D. Tantaroudas, A. Da Ronch, K. J. Badcock, Y. Wang, and R. Palacios, "Model order reduction for control design of flexible free-flying aircraft," in *Proc. AIAA Atmos. Flight Mech. Conf.*, Kissimmee, FL, USA, Jan. 2015, p. 240.

[12] Y. Wang, H. Song, K. Pant, M. J. Brenner, and P. M. Suh, "Model order reduction of aeroservoelastic model of flexible aircraft," in *Proc. 57th AIAA/ASCE/AHS/ASC Struct., Struct. Dyn., Mater. Conf.*, San Diego, CA, USA, Jan. 2016, p. 1222.

[13] W. Su and C. Cesnik, "Flight dynamic stability of a flapping wing micro air vehicle in hover," in *Proc. 52nd AIAA/ASME/ASCE/AHS/ASC Struct., Struct. Dyn. Mater. Conf.*, Denver, CO, USA, Apr. 2011, p. 209.

[14] W. Wang, X. Zhu, Z. Zhou, and J. Duan, "A method for nonlinear aeroelasticity trim and stability analysis of very flexible aircraft based on co-rotational theory," *J. Fluid Struct.*, vol. 62, pp. 209–229, Apr. 2016.

[15] P. Qi, Y. Wang, X. Zhao, R. Palacios, and A. Wynn, "Trajectory control of a very flexible flying wing," in *Proc. Amer. Control Conf. (ACC)*, Seattle, WA, USA, May 2017, pp. 4480–4485.

[16] R. G. Cook, R. Palacios, and P. Goulart, "Robust gust alleviation and stabilization of very flexible aircraft," *AIAA J.*, vol. 51, no. 2, pp. 330–340, Feb. 2013.

[17] F. Li, Y. Wang, and A. Da Ronch, "Flight testing an adaptive feedforward controller for gust loads alleviation on a flexible aircraft," in *Proc. AIAA Atmos. Flight Mech. Conf.*, Washington, DC, USA, Jun. 2016, p. 3100.

[18] W. Fan, H. H. Liu, and R. Kwong, "Gust load alleviation control for a flexible aircraft with loss of control effectiveness," in *Proc. AIAA Guid., Navigat., Control Conf.*, Grapevine, TX, USA, Jan. 2017, p. 1721.

[19] S. Haghighat, H. H. T. Liu, and J. R. R. A. Martins, "Model-predictive gust load alleviation controller for a highly flexible aircraft," *J. Guid., Control, Dyn.*, vol. 35, no. 6, pp. 1751–1766, Nov. 2012.

[20] H. G. Giesseler, M. Kopf, P. Varutti, T. Faulwasser, and R. Findeisen, "Model predictive control for gust load alleviation," in *Proc. 4th IFAC Nonlinear Model Predictive Control Conf., Int. Federation Autom. Control (IFAC)*, Noordwijk, The Netherlands, Aug. 2012, pp. 27–32.

[21] T. Hu and Z. Lin, "Composite quadratic Lyapunov functions for constrained control systems," *IEEE Trans. Autom. Control*, vol. 48, no. 3, pp. 440–450, Mar. 2003.

[22] H. Zhang, A. Song, H. Li, and S. Shen, "Novel adaptive finite-time control of teleoperation system with time-varying delays and input saturation," *IEEE Trans. Cybern.*, early access, Jul. 18, 2019, doi: 10.1109/TCYB.2019.2924446.

[23] Z. Zhao, X. He, Z. Ren, and G. Wen, "Boundary adaptive robust control of a flexible riser system with input nonlinearities," *IEEE Trans. Syst., Man, Cybern. Syst.*, vol. 49, no. 10, pp. 1971–1980, Oct. 2019.

[24] Z. Zhao, C. K. Ahn, and H.-X. Li, "Dead zone compensation and adaptive vibration control of uncertain spatial flexible riser systems," *IEEE/ASME Trans. Mechatronics*, vol. 25, no. 3, pp. 1398–1408, Jun. 2020.

[25] Y. Ren, Z. Zhao, C. Zhang, Q. Yang, and K.-S. Hong, "Adaptive neural-network boundary control for a flexible manipulator with input constraints and model uncertainties," *IEEE Trans. Cybern.*, early access, Oct. 1, 2020, doi: 10.1109/TCYB.2020.3021069.

[26] Z. Chu, X. Xiang, D. Zhu, C. Luo, and D. Xie, "Adaptive trajectory tracking control for remotely operated vehicles considering thruster dynamics and saturation constraints," *ISA Trans.*, vol. 100, pp. 28–37, May 2020.

[27] S. Gao, Y. Jing, X. Liu, and S. Zhang, "Finite-time attitude-tracking control for rigid spacecraft with actuator failures and saturation constraints," *Int. J. Robust Nonlin.*, vol. 30, no. 5, pp. 1903–1937. Dec. 2019.

[28] L. Xu, Y. Lu, B. Chen, H. Shen, and Z. He, "Stability boundary analysis of highly flexible aircraft with control saturation and structural flexibility," *Proc. Inst. Mech. Eng., G, J. Aerosp. Eng.*, vol. 234, no. 6, pp. 1195–1208, Jan. 2020.

[29] T. Alamo, A. Cepeda, and D. Limon, "Improved computation of ellipsoidal invariant sets for saturated control systems," in *Proc. 44th IEEE Conf. Decis. Control*, Seville, Spain, Dec. 2005, pp. 6216–6221.

[30] W. E. Schmitendorf and B. R. Barmish, "Null controllability of linear systems with constrained controls," *SIAM J. Control Optim.*, vol. 18, no. 4, pp. 327–345, Jul. 1980.

[31] M. G. Goman and M. N. Demenkov, "Computation of controllability regions for unstable aircraft dynamics," *J. Guid., Control, Dyn.*, vol. 27, no. 4, pp. 647–656, Jul. 2004.

[32] B. Kouvaritakis, J. R. Gossner, and J. A. Rossiter, "A Priori stability conditions for an arbitrary number of unstable poles," *Automatica*, vol. 32, no. 10, pp. 1441–1446, Oct. 1996.

[33] D. Liu and A. N. Michel, "Null controllability of systems with control constraints and state saturation," *Syst. Control Lett.*, vol. 20, no. 2, pp. 131–139, Feb. 1993.

[34] M. L. Corradini, A. Cristofaro, and F. Giannoni, "An iterative approach for the description of null controllable regions of discrete-time linear systems with saturating inputs," in *Proc. 19th Medit. Conf. Control Autom. (MED)*, Corfu, Greece, Jun. 2011, pp. 96–101.

[35] T. Hu, *Analysis and Design of Control Systems With Saturating Actuators*. Virginia Beach, VA, USA: Univ. Virginia, 2001, pp. 11–15.

[36] T. Hu, Z. Lin, and L. Qiu, "Stabilization of exponentially unstable linear systems with saturating actuators," *IEEE Trans. Autom. Control*, vol. 45, no. 6, pp. 973–979, Jun. 2001.

[37] Z. Lin and L. Lv, "Set invariance conditions for singular linear systems subject to actuator saturation," *IEEE Trans. Autom. Control*, vol. 52, no. 12, pp. 2351–2355, Dec. 2007.

[38] R. Fabbri, "Null controllable sets and reachable sets for nonautonomous linear control systems," *Discrete Continuous Dyn. Syst.*, vol. 9, no. 4, pp. 1069–1094, 2016.

[39] M. Schulze Darup and M. Monnigmann, "Null-controllable set computation for a class of constrained bilinear systems," in *Proc. Eur. Control Conf. (ECC)*, Zurich, Switzerland, Jul. 2013, pp. 2758–2763.

[40] T. Homer, M. Mahmood, and P. Mhaskar, "A trajectory-based method for constructing null controllable regions," *Int. J. Robust Nonlinear Control*, vol. 30, no. 2, pp. 776–786, Jan. 2020.

[41] T. Homer and P. Mhaskar, "Utilizing null controllable regions to stabilize input-constrained nonlinear systems," *Comput. Chem. Eng.*, vol. 108, pp. 24–30, Jan. 2018.

[42] P. Mhaskar, N. H. El-Farra, and P. D. Christofides, "Stabilization of nonlinear systems with state and control constraints using Lyapunov-based predictive control," *Syst. Control Lett.*, vol. 55, no. 8, pp. 650–659, Aug. 2006.

[43] M. Mahmood and P. Mhaskar, "Enhanced stability regions for model predictive control of nonlinear process systems," *AIChE J.*, vol. 54, no. 6, pp. 1487–1498, Jun. 2008.

[44] J. R. Hammerton, W. Su, G. Zhu, and S. S.-M. Swei, "Optimum distributed wing shaping and control loads for highly flexible aircraft," *Aerosp. Sci. Technol.*, vol. 79, pp. 255–265, Aug. 2018.

[45] W. Su, S. S.-M. Swei, and G. G. Zhu, "Optimum wing shape of highly flexible morphing aircraft for improved flight performance," *J. Aircr.*, vol. 53, no. 5, pp. 1305–1316, Sep. 2016.

[46] W. Su and C. E. S. Cesnik, "Dynamic response of highly flexible flying wings," *AIAA J.*, vol. 49, no. 2, pp. 324–339, Feb. 2011.

[47] L. Xu, Y. Lu, Z. He, R. Lv, and C. Xue, "Flight dynamics modeling and analysis of high aspect ratio flexible aircraft," in *Proc. 15th Int. Bhurban Conf. Appl. Sci. Technol. (IBCAST)*, Islamabad, Pakistan, Jan. 2018, pp. 105–119.

[48] D. A. Peters and M. J. Johnson, "Finite-state airloads for deformable airfoils on fixed and rotating wings," in *Proc. Aeroelasticity Fluid/Struct. Interact., Amer. Soc. Mech. Eng.*, New York, NY, USA, Nov. 1994, pp. 1–28.

[49] D. A. Peters, S. Karunamoorthy, and W.-M. Cao, "Finite state induced flow models. I–two-dimensional thin airfoil," *J. Aircr.*, vol. 32, no. 2, pp. 313–322, Mar. 1995.

[50] M. J. Patil and D. H. Hodges, "Flight dynamics of highly flexible flying wings," *J. Aircr.*, vol. 43, no. 6, pp. 1790–1798, Nov. 2006.

[51] J. Zhang and J. Xiang, "Optimum distributed Optimum distributed tatic and dynamic characteristics of coupled nonlinear aeroelasticity and flight dynamics of flexible aircraft," *Acta Aeronautica Astronautica Sinica*, vol. 32, no. 9, pp. 1569–1582, Sep. 2011.

[52] M. J. Dillsaver, "Gust response and control of very flexible aircraft," Ph.D. dissertation, University of Michigan, Ann Arbor, MI, USA, 2013.

[53] T. Hu, Z. Lin, and L. Qiu, "An explicit description of null controllable regions of linear systems with saturating actuators," *Syst. Control Lett.*, vol. 47, no. 1, pp. 65–78, Sep. 2002.

[54] T. Hu and Z. Lin, *Control Systems With Actuator Saturation: Analysis and Design*. Boston, MA, USA: Birkhäuser, 2000.

[55] Y. Wang, A. Wynn, and R. Palacios, "Nonlinear aeroelastic control of very flexible aircraft using model updating," *J. Aircr.*, vol. 55, no. 4, pp. 1551–1563, Jul. 2018.
[56] D. Sanghi, C. Riso, C. E. Cesnik, and F. Vetrano, "Impact of control-surface flexibility on the dynamic response of flexible aircraft," in *Proc. AIAA Scitech Forum*, Orlando, FL, USA, Jan. 2020, p. 1185.

LIANG XU (Member, IEEE) received the B.S. degree in automation from Nanjing Normal University, China, in 2011. He is currently pursuing the Ph.D. degree in guidance, navigation and control with the Nanjing University of Aeronautics and Astronautics, Nanjing, China. His research interests include flight dynamic modeling and control design.

RUI CAO was born in Shangqiu, Henan, China, in 1994. She is currently pursuing the Ph.D. degree in navigation, guidance, and control. Her research interests include control design, trajectory optimization, and system identification.

YANBIN LIU was born in 1980. He received the B.S. degree from Central South University, China, in 2002, and the Ph.D. degree in guidance, navigation, and control with the Nanjing University of Aeronautics and Astronautics, Nanjing, in 2007. He is currently an Associate Professor with the Academy of Astronautics, Nanjing University of Aeronautics and Astronautics. His research interests include modeling and control of complex systems and flight control design.

YUPING LU was born in 1957. He received the M.S. degree from the Nanjing University of Aeronautics and Astronautics, in 1985. He is currently a Professor with the College of Automation Engineering, Nanjing University of Aeronautics and Astronautics. His research interests include modeling and control of complex systems, modern flight control, modeling and control of morphing aircraft, and hypersonic vehicle.